View metadata, citation and similar papers at core.ac.uk

brought to you by CORE

provided by Open Research Exeter

The Astrophysical Journal, 831:147 (15pp), 2016 November 10 doi:10.3847/0004-637X/831/2/147

© 2016. The American Astronomical Society. All rights reserved.

MODELING DUST EVOLUTION IN GALAXIES WITH A MULTIPHASE, INHOMOGENEOUS ISM

Svitlana Zhukovska[1], Clare Dobbs[2], Edward B. Jenkins[3], and Ralf S. Klessen[4]
[1] Max-Planck-Institut für Astrophysik, Karl-Schwarzschild-Str. 1, D-85741 Garching, Germany
[2] University of Exeter, Stocker Road, Exeter EX4 4QL, UK
[3] Princeton University Observatory, Princeton, NJ 08544-1001, USA
[4] Zentrum für Astronomie der Universität Heidelberg, Institut für Theoretische Astrophysik, Albert-Ueberle-Str. 2, D-69120 Heidelberg, Germany
Received 2016 July 6; revised 2016 August 12; accepted 2016 August 16; published 2016 November 3

ABSTRACT

We develop a model of dust evolution in a multiphase, inhomogeneous interstellar medium (ISM) using hydrodynamical simulations of giant molecular clouds in a Milky Way–like spiral galaxy. We improve the treatment of dust growth by accretion in the ISM to investigate the role of the temperature-dependent sticking coefficient and ion–grain interactions. From detailed observational data on the gas-phase Si abundances [Si_{gas}/H] measured in the local Galaxy, we derive a relation between the average [Si_{gas}/H] and the local gas density n(H) that we use as a critical constraint for the models. This relation requires a sticking coefficient that decreases with the gas temperature. The relation predicted by the models reproduces the slope of −0.5 for the observed relation in cold clouds, which is steeper than that for the warm medium and is explained by dust growth. We find that growth occurs in the cold medium for all adopted values of the minimum grain size a_{min} from 1 to 5 nm. For the classical cutoff of $a_{min} = 5$ nm, the Coulomb repulsion results in slower accretion and higher [Si_{gas}/H] than the observed values. For $a_{min} \lesssim 3$ nm, the Coulomb interactions enhance the growth rate, steepen the slope of the [Si_{gas}/H]–n(H) relation, and provide a better match to observations. The rates of dust re-formation in the ISM by far exceed the rates of dust production by stellar sources. After the initial 140 Myr, the cycle of matter in and out of dust reaches a steady state, in which the dust growth balances the destruction on a similar timescale of 350 Myr.

Key words: dust, extinction – Galaxy: evolution – ISM: abundances

1. INTRODUCTION

A fraction of metals in the interstellar medium (ISM) of galaxies in both the local and high-redshift universe resides in tiny refractory solid particles or dust grains (Dorschner & Henning 1995). Interstellar dust constitutes less than 1% of the ISM by mass, but it has manifold impact on the physics and chemistry of the ISM. Because dust locks some elements away from the gas phase, it reduces abundances of important gas coolants such as C^+ and Si^+ (Bekki 2015b; McKinnon et al. 2016). One of the most important roles of interstellar grains is that they facilitate the formation of molecular hydrogen (H_2) on their surfaces (Hollenbach & Salpeter 1971). The H_2 molecule is the main component of molecular clouds, which are the cradle of star formation in most of the universe (Klessen & Glover 2016, p. 85). Dust absorbs ultraviolet emission from young massive stars and reemits it in the infrared, so the spectral energy distribution from dust is one of the primary indicators of star formation (Calzetti 2013). Moreover, continuum emission from interstellar dust is a commonly used tracer of cold gas in galaxies (e.g., Santini et al. 2014).

Despite the utmost importance of interstellar dust for the ISM evolution, high-resolution numerical simulations of the ISM do not yet follow dust evolution. It is commonly assumed that dust abundance is scaled with metallicity and that the scaling factor, grain size distribution, and chemical composition have the average characteristics of dust in the local Galaxy (e.g., Walch et al. 2015, and references therein). Galactic-scale chemodynamical models consider the dependence of galactic evolution on dust by including H_2 molecule formation on grain surfaces, but they follow the evolution of metallicity only and assume a fixed dust-to-metal ratio (e.g., Christensen et al. 2012; Forbes et al. 2016, and references therein). Hu et al. (2016) recently investigated how the choice of dust-to-metal ratio value affects the evolution of dwarf galaxies through the photoelectric heating process, keeping other dust properties fixed.

There is strong observational evidence that cosmic dust properties are not universal. Rémy-Ruyer et al. (2014) showed that there is large scatter in the observed dust-to-gas ratio versus metallicity relation in local galaxies. Moreover, metal-poor dwarf galaxies tend to have lower dust-to-metal ratios compared to normal spiral galaxies. Recently, infrared (IR) and far-IR surveys of dust emission opened a new venue to probe the spatial variations of dust properties on a small scale. Roman-Duval et al. (2014) analyzed the IR emission maps of the Magellanic Clouds combined with various gas surveys and found large variations in the gas-to-dust ratio that are strongly correlated with the dust surface density distribution. Recently, the far-IR emission survey with the *Planck Satellite* discovered similar variations of the gas-to-dust ratio, both from cloud to cloud and within regions of individual clouds in the Milky Way (Reach et al. 2015). Estimation of the true values of the dust-to-gas ratio at high surface densities is a challenging task since different effects may cause variations of the apparent dust-to-gas ratio measured from observations: the possible underestimation of the molecular gas mass because of the presence of CO-dark molecular gas, variations in dust emissivity in the far-IR caused by grain coagulation in dense clouds, and an actual increase of the dust-to-gas ratio due to gas–grain interactions (see Roman-Duval et al. 2014, for discussion). Variations in dust properties from one line of sight to another in the local galaxy are also supported by observations of extinction curves (Fitzpatrick & Massa 2007), dust opacities (Roy et al. 2013), spectral characteristics (Dartois et al. 2004), and interstellar

element gas-phase abundances (Savage & Sembach 1996a; Jenkins 2009). Thus, not only the dust-to-metal ratio but also the composition and the size distribution of interstellar grains can differ from the standard. It is thus crucial to consider dust evolution in the context of modeling the physics and chemistry of the ISM and using dust as a tracer to study the interstellar gas.

The evolution of interstellar dust is incorporated in one-zone models of the chemical evolution of galaxies, which consider dust properties averaged over the entire galaxy or over the vertical direction within concentric rings in spiral galaxies (Dwek & Scalo 1980; Dwek 1998; Hirashita 1999; Calura et al. 2008; Zhukovska et al. 2008; Zhukovska & Gail 2009; Mattsson & Andersen 2012; Asano et al. 2013b; Zhukovska & Henning 2013; de Bennassuti et al. 2014; Hirashita et al. 2015). These models demonstrate that the galactic dust content is mainly determined by the balance between dust destruction in interstellar shocks and dust production by evolved stars and growth by accretion of gas-phase species in the ISM. Given the relatively short timescales of dust destruction in the ISM of a few 10^8 years (Draine & Salpeter 1979; Seab & Shull 1983; Jones et al. 1994, 1996; Serra Díaz-Cano & Jones 2008; Bocchio et al. 2014), dust growth in the ISM becomes the dominant dust source in galaxies on the timescale from a few 100 Myr to a few gigayears (Zhukovska 2014). An accurate treatment of dust growth is therefore important for modeling of interstellar grains. Although simple dust evolution models can describe the average dust properties in these present-day galaxies, they do not consider the complex structure of the ISM and its impact on dust growth rate and are not able to describe the observed variations of dust properties across the ISM phases.

Recently, there have been a few attempts to take into account the evolution of dust in numerical hydrodynamic galaxy simulations. Bekki (2013) included the time evolution of interstellar dust abundances in the chemodynamical model of disk galaxies and made a step forward by coupling it to the galactic evolution via H_2 formation on grain surfaces. The hydrodynamics of interstellar gas is modeled by the smoothed particle hydrodynamics (SPH) method. With the assumption that the dust is coupled to gas, the model considers variations of the dust-to-metal fraction in each gas particle. A disadvantage of the model of Bekki (2013) is the current implementation of dust processing in the ISM in which growth and destruction processes do not depend on the local conditions and occur on constant timescales. In subsequent works, the dependence of the growth timescale on local conditions is included by scaling it with the temperature and density of the particles (Yozin & Bekki 2014; Bekki 2015a). A new, live dust particle model has been presented by Bekki (2015b), who decoupled the gas and dust particles and implemented additional gas–grain interactions and radiation pressure on grains. Recently, dust evolution has been incorporated in the moving-mesh simulation code AREPO and used in zoom-in cosmological simulations of Milky Way–sized galaxies (McKinnon et al. 2016). Their assumptions for the dust model are similar to those outlined in Bekki (2015a), with the exception of the destruction timescale, which they related to the local supernova (SN) rate. While their simulations agree with a number of observables, they overpredict the dust-to-metal ratio in the circumgalactic medium.

The hydrodynamic galactic simulations with evolving dust clearly demonstrate that grains influence the evolution of galaxies, albeit not as strong as SN or active galactic nuclei feedback. However, the existing simulations should be improved in several ways. For example, they do not treat properly the dependence of the growth timescale on metallicity. The timescale of dust growth in the ISM is inversely proportional to the metallicity, resulting in the existence of the critical metallicity for dust growth (e.g., Zhukovska 2008; Zhukovska & Gail 2009; Asano et al. 2013a). While some simulations include a dependence of the growth timescale on the local temperature and density (Bekki 2015a, 2015b; McKinnon et al. 2016), they assume a fixed sticking coefficient over the entire simulation volume. With this assumption, grains can grow by accretion even in the warm or hot gas if they stay a sufficiently long time there (∼1 Gyr). However, sticking of the impinging species to the grain surfaces in this case is unlikely because of their high thermal energies (D'Hendecourt et al. 1985). Moreover, the resolution of cosmological simulations ($\sim 10^5\,M_\odot$) is not sufficient to investigate dense regions where dust growth is expected or to address the observed variations in dust abundances across the ISM phases in the local Galaxy.

In the current study, we describe a new model of dust evolution in the inhomogeneous ISM that includes dust destruction by SN shocks and dust growth in the ISM. We apply the model to study the evolution of the three-dimensional (3D) dust distribution in the local Galaxy using histories of physical conditions from hydrodynamic simulations of the life cycle of giant molecular clouds (GMCs) (Dobbs & Pringle 2013). These simulations have sufficiently high resolution compared to previous works to investigate the changes experienced by grains as they cycle between molecular clouds and the ambient ISM. We substantially improve the treatment of dust growth in the ISM in two ways: by including a temperature-dependent sticking coefficient and Coulomb interactions in calculations of the growth timescale. An advantage of our postprocessing approach is that we can run multiple models to investigate how different model assumptions affect the resulting distribution of dust. Our main goal is to use the analysis of the large amount of element-depletion data measured in the local Galaxy (Jenkins 2009) to constrain the uncertainties in the microphysics of the growth process.

The paper is organized as follows. We describe the initial conditions and main assumptions of these simulations in Section 2. Histories of physical conditions of gas parcels from the hydrodynamic simulations provide input for the dust evolution model. Section 3 presents the formulation of the dust evolution model and our choice of model parameters. Section 4 introduces the data on element depletions in the local Milky Way that provide observational constraints for the model. The results of the model calculations of dust evolution as traced by Si element depletions are presented in Section 5, where we discuss the timescales of dust destruction and formation, the rates of dust growth in the ISM as a function of ambient density, and the distribution of the element-depletion values. Section 5.4 compares the theoretical and observed trends of Si depletion with density. Our conclusions are presented in Section 6.

2. SIMULATIONS OF LIFE CYCLE OF GMCs

In this paper, we utilize a hydrodynamic simulation of the ISM in a spiral Milky Way–like galaxy described in Dobbs & Pringle (2013). The simulation is performed using the

SPH code sphNG (Benz et al. 1990; Bate et al. 1995; Price & Monaghan 2007). The gas in the simulation is subject to a galactic potential. We use a logarithmic galactic potential (Binney & Tremaine 1987), which provides a flat rotation curve, and a two-armed spiral potential from Cox & Gomez (2002). The spiral potential is fixed, with the spiral arms rotating at a constant pattern speed of 19 km s^{-1} kpc, and represents a perturbation of a few percent compared to the logarithmic potential. GMCs form within the arms through a mixture of gravitational and thermal instabilities in the gas and cloud–cloud collisions (Dobbs 2008). There is a total of 8 million gas particles, and each one has a mass $m_{\rm SPH} = 312.5\,M_{\odot}$. The gas is situated within a radius of 10 kpc, and the gas settles into approximately vertical equilibrium after 100 Myr (see Dobbs et al. 2011). The average surface density of the gas is 8 $M_{\odot}$ pc^{-2}.

Cooling and heating of the ISM are incorporated according to Glover & Mac Low (2007), with temperatures representative of a multiphase medium, spanning a range from 50 K to slightly above 10^6 K. The cooling processes include collisional cooling (mainly from C^+, O, and Si^+, but H_2 cooling is also included), and the main heating process is photoelectric heating. The cooling is dependent on metallicity, with the simulation assuming solar metallicity. Although in reality the metallicity would vary with radius, solar metallicity is consistent with the metallicity used in the dust postprocessing, which reflects the properties of the ISM at the solar radius. Self-gravity of the gas is also taken into account.

Stellar feedback is included in the form of supernova feedback once gas reaches a density of 500 cm^{-3} and is gravitationally collapsing. Thermal and kinetic energy are added to particles within a radius R_s of about 15 pc from the densest particle, which is based on the smoothing length at these densities. The energy is inserted according to a snowplow solution; for the exact equations see the appendix of Dobbs et al. (2011). The amount of energy added is calculated as

$$E_{\rm SN} = \frac{\epsilon\, m({\rm H})}{160} 10^{51}\,{\rm erg}, \tag{1}$$

where ϵ is the star-formation efficiency, chosen to be 0.05, m(H) is the mass of molecular hydrogen within R_s, and 10^{51} erg is the energy of one supernova. We adopt a Salpeter IMF such that one supernova occurs for every 160 $M_{\odot}$ of stars formed.

The hydrodynamic simulation then provides input for the dust evolution model, such as the density, temperature, and masses of the SPH particles at each stored snapshot, with a cadence of 1 Myr. The particles that have undergone a recent supernova feedback event can also be identified. In particular, for each supernova event, the dust evolution model uses the total mass of gas where feedback is injected:

$$m_{j,\rm feed} = N_{j,\rm part}\, m_{\rm SPH}, \tag{2}$$

where j refers to the jth feedback event, and $N_{j,\rm part}$ is the number of particles in the jth feedback event (typically around 20). All other assumptions about how the dust evolves in the ISM, and how it is destroyed by feedback, are applied in a postprocessing step according to the dust evolution model described in the next section.

3. DUST EVOLUTION MODEL

In evolved metal-rich systems such as the present-day Milky Way, the timescales of enrichment of the ISM with chemical elements from stars are significantly longer than the timescales of mass transfer between the ISM phases. This allows us to make a number of simplifying assumptions and focus on the dominant sinks and sources of dust. First, we fix the total (dust +gas) element abundances, and, second, we consider the dust production by growth in the ISM and neglect dust input from stars (O'Donnell & Mathis 1997). Additionally, we only include destruction of dust in the interstellar shocks and neglect destruction by star formation since its timescale of 2.5 Gyr is much longer than the current estimates for the dust lifetimes against destruction in shocks. We check the validity of these two latter assumptions by comparing the corresponding dust-formation rates in Section 5.

We model the evolution of dust grains in the ISM by solving numerical differential equations for the degree of condensation, that is, the fraction $f_{\rm X}$ of the key element X in dust. The key element is usually a constituent of the considered dust species that determines the reaction rate for dust growth. It is usually the species with the lowest gas-phase abundance. The $f_{\rm X}$ is related to the logarithmic depletion as $[{\rm X/H}]_{\rm gas} = \log(1 - f_{\rm X})$. The degree of condensation can be converted to the dust mass in a gas parcel as

$$m_{\rm X,dust} = \frac{A_{\rm X}\,\epsilon_{\rm X} X_{\rm H} m_{\rm SPH}}{\xi_{\rm X}} \cdot f_{\rm X}\,, \tag{3}$$

where $\epsilon_{\rm X}$ and $A_{\rm X}$ are the key element abundance and its atomic weight, and $\xi_{\rm X}$ is the mass fraction of the key element in the considered solid, $m_{\rm SPH}$ is the mass of an SPH particle, and $X_{\rm H} = 0.7$ is the hydrogen mass fraction in the gas.

Dust evolution is governed by growth and destruction processes, such that the change of the degree of condensation is

$$\frac{df_{\rm X}}{dt} = \left(\frac{df_{\rm X}}{dt}\right)_{\rm gr} + \left(\frac{df_{\rm X}}{dt}\right)_{\rm dest}. \tag{4}$$

3.1. Growth in the ISM

The mechanism of grain growth in the ISM is not fully understood. It has been suggested that accretion of gas-phase species on silicate and carbonaceous grains occurs selectively to keep them as two distinct populations (see discussion in Draine 2009). We therefore model the evolution of silicate dust independently of carbon dust. Note that, in the present work, we investigate the accretion of refractory elements on the grains that proceeds prior to the accretion of complex ice mantles and coagulation in dense cores of molecular clouds (e.g., Joseph et al. 1986; Weingartner & Draine 1999; Voshchinnikov & Henning 2010).

One-zone dust evolution models usually assume that dust growth occurs in molecular clouds based on their higher densities and consequently shorter collision timescales of gas-phase species with grain surfaces compared to the diffuse medium (Dwek 1998; Zhukovska et al. 2008). We relax this assumption to include possible dust growth in the cold neutral medium (CNM), defined according to the gas temperature range of 30–300 K (e.g., Mihalas & Binney 1981).

The change of the degree of condensation owing to dust growth in the ISM by collisions of gas-phase species with the

grain surfaces is (Zhukovska et al. 2008)

$$\left(\frac{df_{\rm X}}{dt}\right)_{\rm gr} = \frac{1}{\tau_{\rm gr}} f_{\rm X}(1 - f_{\rm X}). \quad (5)$$

Here $\tau_{\rm gr,X}$ is the growth timescale of a given dust species:

$$\tau_{\rm gr,X}^{-1} = \frac{3\alpha_{\rm X}\epsilon_{\rm X} m_{\rm X}}{\rho_d \xi_{\rm X} \langle a\rangle_3} \upsilon_{\rm th,X} n_{\rm H}, \quad (6)$$

where $\alpha_{\rm X}$ is the sticking coefficient that expresses the probability of sticking of the growth species in collision with the surface, and ρ_d is the density of the solid. The thermal velocity $\upsilon_{\rm th,X}$ and the number density of the gas $n_{\rm H}$ are determined by the local conditions recorded in the particle histories. The average grain radius is

$$\langle a\rangle_3 = \langle a^3\rangle / \langle a^2\rangle, \quad (7)$$

where

$$\langle a^l\rangle \sim \int dn_{\rm gr}(a)/da\, a^l da \quad (8)$$

is the lth moment of the grain size distribution $dn_{\rm gr}(a)/da$ defined so that $dn_{\rm gr}(a)$ is the number of grains with radii from a to $a + da$.

In the diffuse ISM, most of the key species are singly ionized, so electrostatic interactions can enhance or reduce accretion rates, depending on the grain charge. To include this effect of Coulomb interactions in our model, we adopt the enhancement factor $D(a)$ from the work of Weingartner & Draine (1999) calculated for the standard interstellar UV radiation field, collisions with singly ionized gas species, and the grain charge distribution described in Weingartner & Draine (2001). We include enhancement effects in the CNM using a modified average grain radius in Equation (6):

$$\langle a\rangle_3 = \langle a^3\rangle / \int \frac{dn_{\rm gr}(a)}{da} a^2 D(a) da, \quad (9)$$

where the electrostatic factor $D(a)$ accounts for the change in the cross section of an interaction between ion and grain. For neutral particles in MCs, $D(a) = 1$.

The timescale of dust re-formation in the ISM is defined as

$$\tau_{\rm form} = \frac{M_{\rm dust}}{\dot{M}_{\rm dust,gr}}, \quad (10)$$

which for the simulations with equal-mass particles can be written using summations over all particles:

$$\tau_{\rm X,form} = \sum_{i=1}^{N_{\rm tot}} f_{{\rm X},i} \Big/ \sum_{i=1}^{N_{\rm tot}} \left(\frac{df_{{\rm X},i}}{dt}\right)_{\rm gr}. \quad (11)$$

We assume that the dust mass grows in the quiescent ISM, and we exclude the gas particles that undergo the SN feedback event described in the next section.

3.2. Dust Destruction in SN Shocks

Sputtering of grains in high-velocity shocks ($\gtrsim$100 km s^{-1}) is the main mechanism of dust destruction in the ISM. The large-scale simulations used in this work do not resolve the scale on which gas is shocked to high velocities, so our approach to calculations of dust destruction utilizes the existing SN energy feedback scheme described in Section 2.

In each feedback event, the energy from SNe is equally distributed between the gas particles with the total mass $m_{j,\rm feed}$ given by Equation (1). In the same feedback event, dust is completely destroyed in a mass of gas $m_{\rm cleared}$, which for the homogeneous ambient medium is defined as (Dwek & Scale 1980)

$$m_{\rm cleared}(n_0) = \int_{\upsilon_0}^{\upsilon_f} \varepsilon(\upsilon_s, n_0) \left|\frac{dM_s(\upsilon_s, n_0)}{d\upsilon_s}\right| d\upsilon_s, \quad (12)$$

where υ_0 and υ_f are the initial and final velocities of the supernova remnant (SNR) expanding into an ambient medium of density n_0, respectively, $\left|\frac{dM_s(\upsilon_s, n_0)}{d\upsilon_s}\right| d\upsilon_s$ is the mass of gas swept up by a shock with velocity in the range of $[\upsilon_s, \upsilon_s + d\upsilon_s]$, and ε is the degree of dust destruction in a gas parcel shocked to the velocity υ_s. To calculate $m_{\rm cleared}$ for each SN remnant, we use Equation (12) together with an analytical expression for $M_s(\upsilon_s, n_0)$ given by Dwek et al. (2007), which describes the adiabatic expansion and pressure-driven snowplow stages of the SNR evolution.

With the resolution of our hydrodynamic simulations, $m_{\rm cleared}$ is lower than $m_{j,\rm feed}$. We therefore make two assumptions that allow us to simplify the treatment of dust destruction. We approximate the total dust mass destroyed in the jth event by $m_{\rm cleared}$ and assume the dust content is reduced equally in all affected gas particles by a fraction

$$\eta_{j,\rm dest} = \frac{m_{\rm cleared}}{m_{j,\rm feed}}. \quad (13)$$

The change in the condensation fraction in each gas particle in the jth feedback event is $-\eta_{j,\rm dest} f_{\rm X}$. The change of condensation degree in a gas parcel that experienced the jth feedback event is

$$\left(\frac{df_{\rm X}}{dt}\right)_{\rm dest}^{\rm feed} = -\frac{\eta_{j,\rm dest} f_{\rm X}}{\Delta t}, \quad (14)$$

where Δt is the time step following the SN explosion. By using Equation (3) and summing over all particles affected by the total $N_{\rm feed}$ feedback events in GMCs, we derive the total dust mass destruction rate

$$\left(\frac{dM_{\rm X,dust}}{dt}\right)_{\rm dest}^{\rm feed} = -\frac{A_{\rm X}\epsilon_{\rm X} X_{\rm H} m_{\rm SPH}}{\xi_{\rm X}} \sum_{i=1}^{N_{\rm feed}} \sum_{j=1}^{N_{j,\rm part}} \frac{\eta_{j,\rm dest} f_{{\rm X},i,j}}{\Delta t_{i,j}}, \quad (15)$$

where $N_{\rm feed}$ is the total number of feedback events that occurred between two subsequent snapshots.

The current implementation of stellar feedback in our simulations neglects such forms of stellar feedback as stellar winds and radiation, prostellar jets, and SNe exploding in low-density regions. The impact of different mechanisms of stellar feedback on the dynamics of the ISM is discussed by Walch et al. (2015). Among the different processes, blast waves in the low-density gas are most important for dust destruction (McKee 1989; Draine 1990). Observationally it has been determined that 20%–25% of OB stars belong to the field stars and will likely explode in the diffuse ISM (Oey & Lamb 2012). Without an account of these SNe we may underestimate the overall dust destruction in the ISM. To investigate their effect on the outcome of the simulations, we also run models with an additional term in the total destruction rate for all particles with

Table 1
Basic Data Used in Model Calculations

Physical quantity	Value
Key element	Si
$A_{\rm si}$	28
$\xi_{\rm Si}$	0.165
Solid material density ρ_d (g cm^{-3})	3.13
Element abundance $\epsilon_{\rm Si}$ (10^{-5})	3.24
Initial depletion [Si$_{\rm gas}$/H]	−0.5
Threshold for destruction in diffuse gas $n_{\rm dest}^{\rm diff}$ (cm^{-3})	1
Timescale for destruction in diffuse gas $\tau_{\rm dest}^{\rm diff}$ (Gyr)	0.1
Carbon-to-silicate mass ratio	0.5

Table 2
Average Grain Radius $\langle a\rangle_3$ Adopted in Model Calculations for the Selected Minimum Sizes of the MRN Grain Size Distribution

$a_{\rm min}$ (nm)	$\langle a\rangle_3$ (nm)	
	Normal[a]	Enhanced[b]
1	15.8	0.8
3	27.4	7.7
5	35.4	48.2

Notes.
[a] The average grain radius derived from Equation (7).
[b] $\langle a\rangle_3$ derived from Equation (9) for the enhancement factor $D(a)$ for silicate grains in the CNM.

density below $n_{\rm dest}^{\rm diff} = 1$ cm^{-3}, adopted as an upper limit for the diffuse ISM:

$$\left(\frac{df_{\rm X}}{dt}\right)_{\rm dest}^{\rm diff} = -\frac{f_{\rm X}}{\tau_{\rm dest}^{\rm diff}}, \quad (16)$$

where $\tau_{\rm dest}^{\rm diff}$ is the timescale to destroy all dust in the diffuse medium. This destruction rate is added on each time step only to those particles that are not affected by current stellar feedback events in GMCs. Note that in order to derive the timescale to destroy all grains in the ISM by this process, $\tau_{\rm dest}^{\rm diff}$ has to be divided by the mass fraction of diffuse gas.

3.3. Model Parameters

To solve equations for the condensation degree numerically, we need to make assumptions about the main properties of dust. For the total (gas+dust) chemical composition, we adopt solar metallicity $Z_\odot = 0.015$ and element abundance ratios from Lodders et al. (2009, pp. 712–770). In this work, we focus on the growth of silicate dust, assuming that Si is the key species in silicate growth. For the adopted olivine-type composition ($MgFeSiO_4$) of silicates, the mass fraction of Si in dust is $\xi_{\rm Si} = 0.165$. All physical quantities used in the calculations are summarized in Table 1.

For the initial dust abundance, we take a constant value for all gas particles $f_{\rm Si} = 0.68$ ([Si$_{\rm gas}$/H] $= -0.5$). This is on the lower limit of the general depletion level in the warm neutral medium (WNM) derived by Savage & Sembach (1996b) and somewhat lower than the value [Si$_{\rm gas}$/H] $= -0.36$ suggested by the depletion data from work by Jenkins (2009) (see Section 4). This value is consistent with the Si abundance required by models for extinction, emission, and polarization of light by dust in the diffuse ISM in the solar neighborhood (Siebenmorgen et al. 2014). We intentionally take low initial dust abundances for all particles with higher density to explore how the system reaches the balance between destruction and production processes.

Efficiencies of grain destruction ε for different dust species are obtained from extensive numerical calculations of grain evolution in the shocked gas. For $\varepsilon(\upsilon)$, we adopt the values from works by Jones et al. (1994) and Jones et al. (1996) derived for steady shock models.

The dust growth rate depends on the choice of the grain size distribution through Equation (6). For simplicity, we apply a commonly used power-law distribution $dn_{\rm gr}(a)/da \sim a^{-3.5}$ (Mathis et al. 1977, hereafter called MRN), which runs from $a_{\rm min} = 5$ nm to $a_{\rm max} = 250$ nm. The value $a_{\rm min} = 3$ nm is used in our reference models. To investigate how the minimum grain size affects our results, we perform additional model calculations for $a_{\rm min} = 1$ and 5 nm and discuss them in Section 5.6. The corresponding values of the average grain size are listed in Table 2.

3.3.1. Description of the Models

The basic name of our models is "MRN*x*nm," where x is the minimum grain size in nm and MRN indicates that all models assume an MRN grain size distribution. We add "E" at the beginning of the name of the models in which the average timescale of accretion $\langle a\rangle_3$ is calculated accounting for electrostatic interactions due to ion–grain collisions in the CNM, otherwise a fixed value of $\langle a\rangle_3$ is used in all phases (Table 2). The models with additional destruction in the diffuse medium as described in Section 3.2 are denoted with an additional prefix "C." The model ECMRN3nm is our best-fit model for which most of the analysis is given below.

3.3.2. Sticking Coefficient

The sticking coefficient α is the major source of uncertainty of our model. One-zone dust evolution models usually assume that growth occurs in molecular clouds and that key species colliding with the grain surface stick perfectly so that $\alpha = 1$ (O'Donnell & Mathis 1997; Zhukovska et al. 2008; Asano et al. 2013b; see also Weingartner & Draine 1999). Hirashita & Kuo (2011) adopt a more conservative value of $\alpha = 0.3$. A constant value of α has also been adopted in recent numerical simulations of galaxies with dust evolution (e.g., Bekki 2015b; McKinnon et al. 2016). This assumption is justified at low gas temperatures $T_{\rm gas} \approx 10$–100 K and dust temperatures $T_{\rm dust} \approx 10$ K because the kinetic energy of incident Si atoms is significantly lower than their binding energy on the surface (e.g., D'Hendecourt et al. 1985). It may, however, overestimate the dust growth rate in the warm medium in hydrodynamical simulations.

In this work, we include gas–grain interactions in the diffuse ISM where most of the silicon is singly ionized. The sticking coefficient for Si^+ on a silicate surface is not known. Watson & Salpeter (1972) discuss possible outcomes of the interaction between a positive ion and a negatively charged grain. They point out that when an ion approaches the grain surface, one of the electrons in the grain may tunnel through the work function and neutralize the ion before it reaches the surface. The probability that the atom will remain on the surface upon collision increases dramatically if it can be chemisorbed (Watson & Salpeter 1972). This possibility is supported by

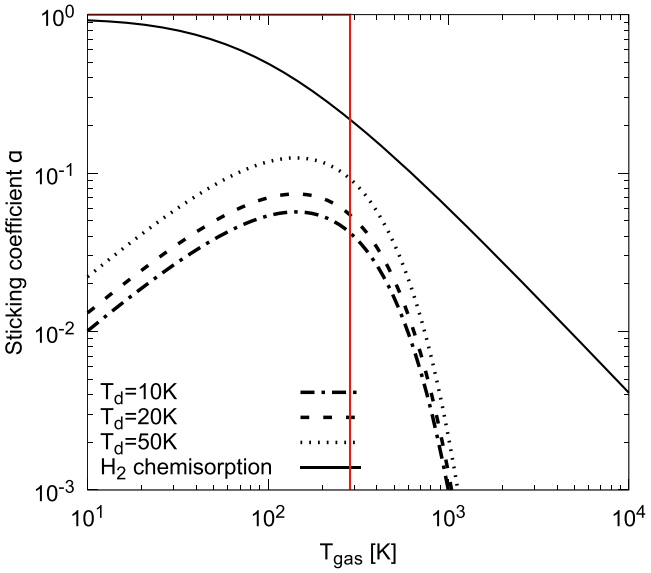

Figure 1. Sticking coefficient for H_2 chemisorption on the silicate surface derived by Chaabouni et al. (2012) (solid line) and that for physisorption derived by Leitch-Devlin & Williams (1985) for dust temperatures 10, 20, and 50 K (dash-dotted, dashed, and dotted lines, respectively). Step function (solid red line) shows α assumed in the reference models.

recent experiments in Jena that demonstrate that adsorbed species can form chemical bonds characteristic of silica and silicates at substrate temperatures of 10 K without an activation barrier (Krasnokutski et al. 2014; Rouillé et al. 2014).

The sticking coefficient depends on many parameters, including the poorly understood surface properties of interstellar grains. With these uncertainties, the observed relation between interstellar depletions and gas density may provide an observational constraint for the choice of α. To this end, we investigate various choices of the sticking coefficient: (1) a fixed value $\alpha = 1$ for $T_{\rm gas} \leqslant 300$ K and $\alpha = 0$ for $T_{\rm gas} > 300$ K, (2) a fixed value $\alpha = 1$ for all temperatures, (3) an experimentally measured α for chemisorption of H_2 molecules on silicate surfaces by Chaabouni et al. (2012), and (4) $\alpha(T_{\rm gas}, T_{\rm dust})$ from theoretical calculations of physisorption performed by Leitch-Devlin & Williams (1985). In the absence of estimates of α for physisorption of Si on silicate grain surfaces, we provisionally adopt the data for carbon atoms arriving on a graphite lattice from the work by Leitch-Devlin & Williams (1985), in the functional form derived by Grassi et al. (2011). The dust temperature is fixed to 20 K.

We deem the temperature dependence of the sticking coefficient measured by Chaabouni et al. (2012) more plausible than that of the α derived by Leitch-Devlin & Williams (1985) (Figure 1). The former increases at low gas temperatures and approaches one at $T_{\rm gas} \lesssim 10$ K, while the latter peaks at $T_{\rm gas} \approx 200$ K and decreases at lower gas temperatures. However, after initial testing and comparison of model predictions with the observational constraints discussed in Section 4, we assume the case (1) with a simple step function dependence of α on $T_{\rm gas}$ for the reference model. It restricts the growth with temperature and does not depend on the exact shape of $\alpha(T_{\rm gas})$ that has yet to be determined by future experiments.

As we will show later in this paper, the assumption of $\alpha = 1$ for all temperatures results in too-high average depletions compared to the range of values derived from depletion studies and should not be used.

4. DEPLETION OF ELEMENTS IN THE ISM

In this section, we discuss the observational data used to constrain our model. Interstellar dust abundances can be studied by analyzing the gas-phase abundances of refractory elements, assuming that the elements missing from the gas are locked into the dust. The abundances of free atoms and ions in space can be determined by analyzing absorption features appearing in the ultraviolet spectra of background stars (Spitzer & Jenkins 1975). The logarithmic depletion of an element X in the ISM is the gas-phase element abundance relative to a reference abundance, for which we adopt the element abundance in the proto-Sun reflected by the present-day photospheric abundance, with an increase of 0.07 dex to account for gravitational settling (Lodders 2003):

$$\left[\frac{\rm X_{gas}}{\rm H}\right] = \log\left(\frac{n_{\rm X}}{n_{\rm H}}\right)_{\rm gas} - \log\left(\frac{n_{\rm X}}{n_{\rm H}}\right)_{\odot}. \quad (17)$$

There are significant variations of interstellar element depletions between different lines of sight, which are probably related to dust evolution driven by local conditions and the recent history of the gas. The observed determinations of element depletions [$\rm Si_{gas}$/H] can therefore be used to validate and provide useful constraints for our model.

One simple quantity commonly used in the interpretation of interstellar element depletions is the average gas density $\langle n({\rm H})\rangle$ along the sight line, defined as the ratio of the column density of hydrogen (both atomic and molecular) to the distance of the background star D:

$$\langle n({\rm H})\rangle = [N_{\rm H} + N_{\rm H_2}]/D. \quad (18)$$

This is a volume-weighted determination of local densities. It has been well established that $\langle n({\rm H})\rangle$ strongly correlates with element depletions (e.g., Joseph et al. 1986; Jenkins 1987; Joseph 1988; Jenkins 2009; Savage & Sembach 1996b; Haris et al. 2016). However, this correlation may be governed more by the relative proportions of some representative high-density material and a very low density gas (Spitzer 1985; Jenkins et al. 1986), rather than an average for the local densities over regions containing mostly neutral hydrogen along the sight line. In reality, the value of $\langle n({\rm H})\rangle$ provides a lower limit for the gas densities associated with measured element depletions, with an understanding that the true average hydrogen density for the measurements may be significantly higher if much of the sight line is filled with fully ionized (and hence invisible) gas.

The outputs from our dust formation models show details on the distributions of Si depletions as a function of local density. The lack of an exact correspondence between $\langle n({\rm H})\rangle$ and representative local densities presents a challenge in making meaningful comparisons of the observed depletions to the dust models.

To derive the relation between [$\rm Si_{gas}$/H] and the mean sight-line density $\langle n({\rm H})\rangle$, we start with the data compiled by Jenkins (2009), which included over 243 lines of sight probing a large range of physical conditions. The sight lines with the extraordinarily high velocities typical of shocked gas were excluded from the analysis. Only stars situated within about 1.5 kpc from

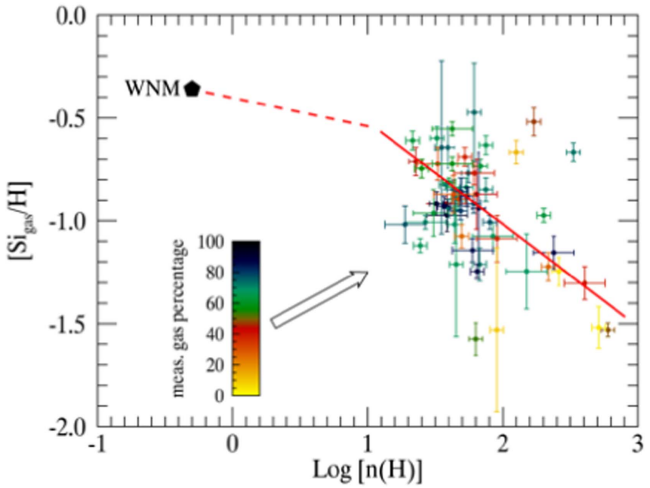

Figure 2. Multiple points with error bars: gas-phase Si abundances [Si_{gas}/H] (Jenkins 2009) vs. the corresponding logarithms of the local gas densities n(H), as inferred from absorption features arising from the C I fine-structure levels in various directions (Jenkins & Tripp 2011). These measurements are indicated with colors that correspond to estimates for the fractions of the total material that were sampled by the fine-structure population ratios. A solid red line indicates the least-squares linear fit to the data. Single black pentagon: an estimate for the representative Si abundance for the warm neutral medium for a value of F_* equal to 0.12 that corresponds to depletions measured by Savage & Sembach (1996a) for this phase.

the solar Galactocentric radius were used for the quantitative analysis, which avoids the possible consequences of the Galactic radial abundance gradient. In the work of Jenkins (2009), the depletions were expressed in terms of a factor designated as F_*, a parameter that characterized the relative strengths of some available element depletions for a given line of sight. Because all of the different element depletions behave in well-defined manners with respect to F_*, this parameter can be used as a proxy to determine the depletion of any particular element (in our case Si), even if that element was not observed for the sight line under consideration. We may express how F_* relates to $\langle n(\mathrm{H})\rangle$ using a linear fit to the data plotted in Figure 16 in Jenkins (2009) and the Si abundance [Si_{gas}/H] as a function of F_* (by the use of Equation (10) in Jenkins (2009)), which allows us to derive the following relation between the gas-phase Si abundance and the average density:

$$[\mathrm{Si_{gas}/H}] = -0.524 \log \langle n(\mathrm{H})\rangle - 1.10. \quad (19)$$

There is a more direct way to probe the local gas density in diffuse cold clouds based on an analysis of the collisional excitation of the fine-structure levels of interstellar neutral carbon. Jenkins & Tripp (2011) investigated the C I absorption lines seen in the spectra of stars recorded in the highest-resolution echelle modes of the Space Telescope Imaging Spectrograph on board the *Hubble Space Telescope*. This investigation included 89 out of the 243 lines of sight from the data sample from Jenkins (2009). Using the estimates of thermal gas pressure and temperature evaluated by Jenkins & Tripp (2011), we calculate the gas densities n_{H} in the interstellar cold clouds and paired them with the gas-phase Si abundances along the same sight lines. The outcomes are shown in Figure 2. The best fit to these results is represented by the equation

$$[\mathrm{Si_{gas}/H}] = -0.497 \log n(\mathrm{H}) - 0.0225, \quad (20)$$

and it is shown as a solid red line in the figure. This outcome is based on minimizing the χ^2 for the errors in both $\log n$(H) and [Si_{gas}/H] using the routine "`fitexy`" (Press et al. 2007).

Because the ionization equilibrium between C I and C II is governed by the local electron density, the measurements of the fine-structure level populations for C I are biased in favor of denser gas, which means that the derived hydrogen densities are restricted to the range from about 10 to 10^3 cm^{-3}. It follows that the WNM is not sampled by the C I because the characteristic densities are much lower. For this reason, we must try to understand empirically how influential this WNM contamination is for our determinations of representative local densities of neutral hydrogen that appear in Figure 2.

For every sight line, Jenkins & Tripp (2011) estimated the fraction of gas that was sampled by the C I fine-structure excitations by examining the absorption profiles of other species in their dominant ionization stages, which could serve as proxies for C II. Based on this information, they stated this sampling fraction in terms of a quantity that they called "fraction of C II observed" (see their Table 3). If this percentage is low, one must conclude that the WNM dominates over the CNM, and this effect could lead to an outcome for the silicon depletion that is less severe than that for the dense region (Savage & Sembach 1996a).

To evaluate the importance of the WNM contributions, we reevaluated the best-fit relationship only for cases where the fraction of C II in the measurable C I velocity range exceeded 50%. The change of the coefficients in Equation (20) was inconsequential.

In their review of interstellar abundances, Savage & Sembach (1996a) stated general values for depletions in the WNM in the Galactic disk, which Jenkins converted to a value for the F_* parameter equal to 0.12, which in turn yields [Si_{gas}/H] = −0.36. We include in Figure 2 a point that shows this level of Si depletion at a location for a typical density of the WNM, $n(H) \approx 0.5$ cm^{-3}. The value n(H) ~ 0.5 cm^{-3} for the representative density is justified by Jenkins (2013); see Section 7.4 of that paper. Gas in the Galactic halo probably represents material that has been shocked and accelerated, and here the Si abundances may be even higher because the grains have been eroded even further.

5. RESULTS

In the following, we present the results of the calculations of dust evolution as traced by Si abundance in the Milky Way–like disk galaxy simulated for 270 Myr. Because our goal is to compare the model predictions with the observed depletion data limited to a few kiloparsecs around the Sun (Jenkins 2009), we select the particles in a ring with galactic radii from 6 to 9 kpc to represent conditions similar to those in the solar neighborhood.

5.1. Dust Production Rates

Our model predicts the rates of destruction and production of silicate dust with a fixed olivine-type composition. If we assume that the carbon-to-silicate dust mass ratio does not vary significantly across the ISM phases, we can estimate the total rates of dust production and destruction in the ISM. We adopt the carbon-to-silicate ratio of 0.5 inferred for interstellar dust in the local diffuse ISM (Dwek 2005).

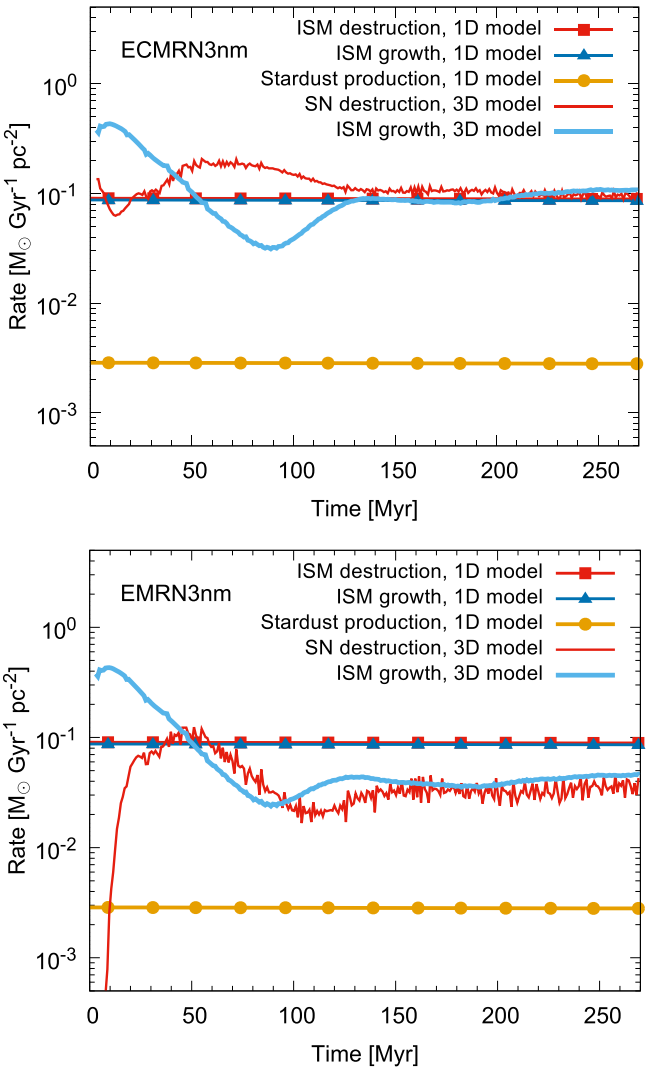

Figure 3. Evolution of rates of dust destruction in the interstellar shocks and production by growth in the ISM (thin red and thick blue lines, respectively). The rates of dust production in the ISM, destruction by SN shocks, and the stardust injection rate from a 1D dust evolution model (Zhukovska et al. 2008) are shown for comparison (lines with solid triangles, squares, and circles, respectively). The top and bottom panels show models with and without additional destruction in the diffuse ISM (ECMRN3nm and EMRN3nm, respectively).

Figure 3 shows the variations of the interstellar dust production and destruction rates per unit of surface area as a function of time after the start of our calculations. On two panels, we show the results for models EMRN3nm and ECMRN3nm, which correspond to the case of dust destruction only by feedback from massive stars in GMCs and the case with the additional destruction in the diffuse medium.

The total dust growth rate is higher at the beginning because of the low values of the initial element depletions in the simulation volume. The initial peak is followed by a dip in the production rate at 90 Myr resulting from the enhanced SN rate (Figure 4) caused by the initial conditions of the hydrodynamic simulations.

Figure 3 illustrates that, after the initial 140 Myr, the cycle of matter in and out of dust reaches a steady state, in which interstellar dust is distributed over the ISM phases in such a way that the dust production rate balances the destruction rate. The destruction and production rates converge to a similar value in the steady state controlled by the destruction timescale. It is about 0.04 $M_\odot$ Gyr^{-1} pc^{-2} for model EMRN3nm, which determines a lower limit for the dust destruction rate and corresponds to destruction only by feedback from massive stars in GMCs. For the ECMRN3nm model, the value of destruction/production rates in the steady state is a factor of 2.5 higher and attains the value of 0.1 $M_\odot$ Gyr^{-1} pc^{-2}.

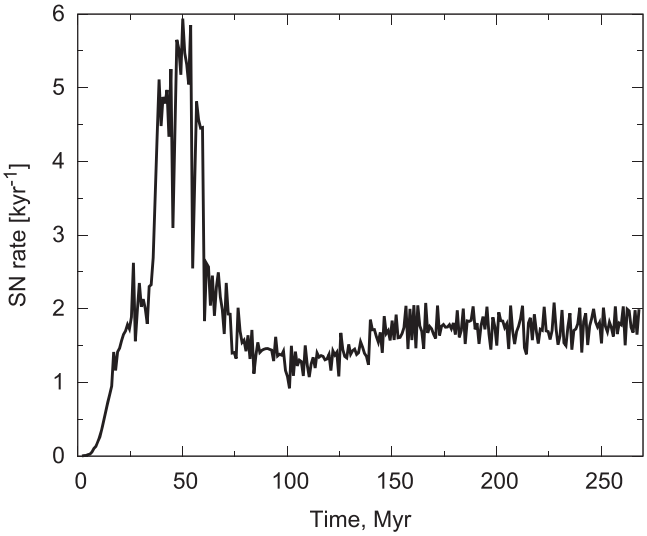

Figure 4. Evolution of the total supernova rate in the simulation volume.

The resulting total rate of dust destruction/ISM growth for the ECMRN3nm model matches remarkably well with the value from a simple one-zone model of chemical evolution of the solar neighborhood with dust derived by Zhukovska et al. (2008). The one-zone model considers the evolution of dust surface densities averaged over the vertical direction as well as in a 1-kpc-wide ring with the solar galactocentric radius. It follows the evolution of dust and gas chemical abundances for 13 Gyr from the primordial chemical abundances to the present-day values. Time variations of the destruction and ISM dust growth rates predicted by the one-zone model are also displayed in Figure 3. For comparison with our results, we take the rates from the one-zone model for the last 270 Myr before the present time. These rates from the one-zone model do not noticeably vary over the considered time span because it is much shorter than the present-day timescale of chemical enrichment.

The one-dimensional dust evolution model also predicts the dust injection rate by asymptotic giant branch (AGB) stars and SNe based on the star-formation history of the solar neighborhood and stellar dust yields described in Zhukovska et al. (2008) and Ferrarotti & Gail (2006). The current rate of dust input from stars is 3×10^{-3} $M_\odot$ Gyr^{-1} pc^{-2} (Figure 3). This is 33 times lower than the dust production rate by ISM growth in our reference model ECMRN3nm. This corroborates our model assumption that growth in the ISM is the dominant dust source in the present-day Milky Way and dust production in stellar winds can be neglected. Note that this assumption does not hold during the early evolution of the Milky Way or in young metal-poor dwarf galaxies (Zhukovska et al. 2008; Zhukovska 2014).

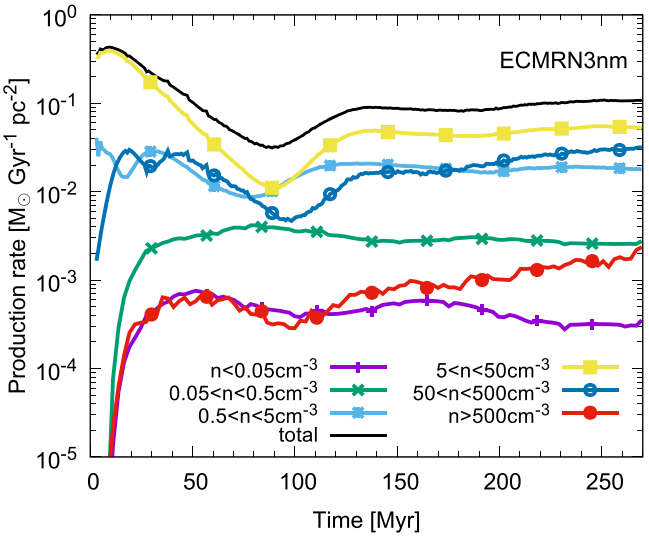

Figure 5. Evolution of dust production rates in the ISM in model ECMRN3nm separated into gas density bins of width of 1 dex from 0.05 to 500 cm^{-3}.

5.1.1. Where Do Interstellar Grains Grow?

To investigate the conditions that favor dust growth in our hydrodynamical simulations, we compare the dust production rates within the logarithmic gas density intervals from 0.05 to 500 cm^{-3} with a step size of 1 dex. The time evolution of the rates in each density bin for the ECMRN3nm model is shown in Figure 5. It demonstrates that most of the growth (49% of the total ISM growth rate) occurs at densities in the range 5 cm^{-3} $< n \leqslant$ 50 cm^{-3}. Gas with density in the range 50 cm^{-3} $< n \leqslant$ 500 cm^{-3} contributes 30%, and more diffuse clouds with 0.5 cm^{-3} $< n \leqslant$ 5 cm^{-3} contribute 17% to the total growth rate, correspondingly. The contribution from the diffuse medium with $n \leqslant$ 0.5 cm^{-3} constitutes only 3% of the total rate. This is not surprising since the growth is limited to $T \leqslant$ 300 K in the reference model.

Our results do not drastically change for models with different temperature-dependent sticking coefficients tested in this work (Leitch-Devlin & Williams 1985; Chaabouni et al. 2012). Compared to a simple step function dependence on temperature in the reference models, the sticking coefficient usually decreases with gas temperatures from the maximum value close to one, similar to the behavior of the data from Chaabouni et al. (2012) shown in Figure 1. Such dependence somewhat reduces the growth rate in the density bin 0.5 cm^{-3} $< n \leqslant$ 5 cm^{-3} and increases it in the next density bin (5 cm^{-3} $< n \leqslant$ 50 cm^{-3}), resulting in very similar values of growth rates in these two bins.

Our simulations do not resolve the dense gas well, so its actual contribution can be higher than the present value of a few percent.

5.2. Timescales of Dust Destruction and Re-formation in the ISM

Figure 6 shows the evolution of the average timescales of silicate dust destruction and re-formation in the ISM derived using the dust production and destruction rates for models ECMRN3nm and EMRN3nm (Figure 3). The early evolution of the dust formation timescale is strongly affected by the initial conditions for both the hydrodynamical simulations and dust abundances. The adopted constant depletion

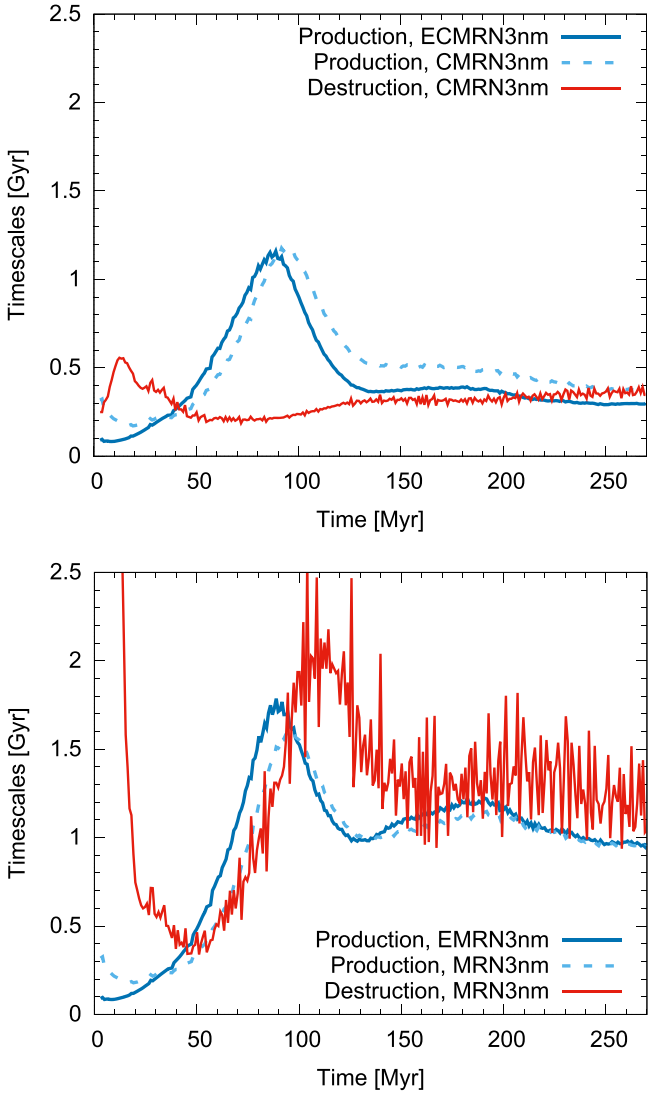

Figure 6. Top panel: evolution of timescales of silicate dust destruction and production by growth in the ISM for model ECMRN3nm (thin red and thick blue lines, respectively). The production rate for model CMRN3nm is shown with the dashed line. Bottom panel: the same for the EMRN3nm and MRN3nm models without additional destruction in the diffuse ISM.

[Si$_{gas}$/H] $= -0.5$ at the onset of the simulations causes a rapid growth phase with a formation timescale of a few hundred megayears. Later on, the growth is slowed down as a consequence of a temporal reduction of the GMC mass fraction by feedback from the initial burst of star formation. This reduction in the star-formation activity manifests in Figure 4 as a dip in the SN rate following the peak corresponding to the initial starburst. Strong feedback from the starburst suppresses the growth in clouds and increases τ_{form} to over 1 Gyr by a time of 90 Myr in both models. However, the steady-state values of the destruction and formation timescales, reached after the balance between disruption and formation of GMCs is established, differ significantly for the two models.

The average timescale of dust destruction τ_{dest} calculated for model ECMRN3nm is three times shorter than for model EMRN3nm and reaches down to 350 Myr. For the adopted low value of the timescale of the destruction rate in the diffuse

medium $\tau_{\rm dest}^{\rm diff} = 100$ Myr, $\tau_{\rm dest}$ is determined by the $\tau_{\rm dest}^{\rm diff}$ and the mass fraction of the diffuse ISM in our simulations, which is about 20%. Efficient destruction in the diffuse phase with a short $\tau_{\rm dest}^{\rm diff}$, resulting in the short lifetime of grains in the ISM, are required for our model to reproduce the mean Si depletion in the diffuse medium. Our results thus reinforce the assumption proposed in earlier studies that sputtering of grains in the diffuse ISM by single SNe is the dominant mechanism of dust destruction (McKee 1989).

When only destruction by SN feedback in GMCs is included (model EMRN3nm), the lifetime of grains in the ISM $\tau_{\rm dest}$ at the end of the simulations reaches 1 Gyr. Model EMRN3nm overpredicts the high depletions of Si in the WNM compared to the observed value, −1 and −0.36, respectively. The value of 350 Myr predicted by model ECMRN3nm at the end of the simulations is 50 Myr lower than the lifetime of silicate grains in the Milky Way estimated by Jones et al. (1996). Following McKee (1989), they combined the observed mass of the ISM and galactic SN rate with their estimate of the $m_{\rm cleared}$ given by Equation (12) resulting from extensive numerical calculations of the dust destruction in the blast wave.

We can also compare the timescale from our simulations with other studies that improved various aspects of the physics of grain destruction in a shock but kept the same simple approach to the grain cycle in the homogeneous ISM. Bocchio et al. (2014), for example, reevaluated the dust lifetimes against destruction using models with a better treatment of the dust dynamics in the shock. With consideration of the uncertainties in the observed mass of the ISM and SN rate, they derived the lifetime of 310 ± 270 Myr for silicate grains, which is very close to the value predicted by our best-fit model. Slavin et al. (2015) proposed much longer lifetimes of silicate grains of 2–3 Gyr. Although they included the hydrodynamical shock evolution in calculations of the destruction efficiency $\varepsilon(v_s, n_0)$, the new value of $m_{\rm cleared}$ from their work is not very different from that in the previous works. The main reason for their longer $\tau_{\rm dest}$ is the new estimates of the total gas mass and SN rate from recent observations.

The average dust-formation timescale in the ISM $\tau_{\rm form}$ for models with enhanced collision rates of cations with grains in the CNM is not very different from those without them (Figure 6). The differences are larger for models with additional destruction in the diffuse medium. They can be explained by differences in $\tau_{\rm gr}$ and the element depletion levels in these models. The growth timescale in the CNM $\tau_{\rm gr}$ is four times shorter for model ECMRN3nm, which results in rapid depletion of Si from the gas phase at higher levels than in model CMRN3nm. Since $\tau_{\rm form}$ increases with $\tau_{\rm gr}$ in individual gas particles and decreases with their element condensation fractions $f_{\rm Si}$ (see Equations (5) and (6)), the interplay between these two factors determines the ratio of $\tau_{\rm form}$ predicted by the models with and without enhanced collision rates.

5.3. Distribution of Si Depletion with Density

We analyze the complex distribution of Si depletion values in the simulation volume by means of mass-weighted probability density functions (PDFs) calculated in logarithmically equal gas density intervals. Figure 7 displays the PDFs of the final distribution of Si depletions for the logarithmic gas density intervals from 0.05 to 500 cm^{-3} with steps of 1 dex. All PDFs are normalized to the total mass of gas. The main feature of the derived distributions is broad asymmetric profiles

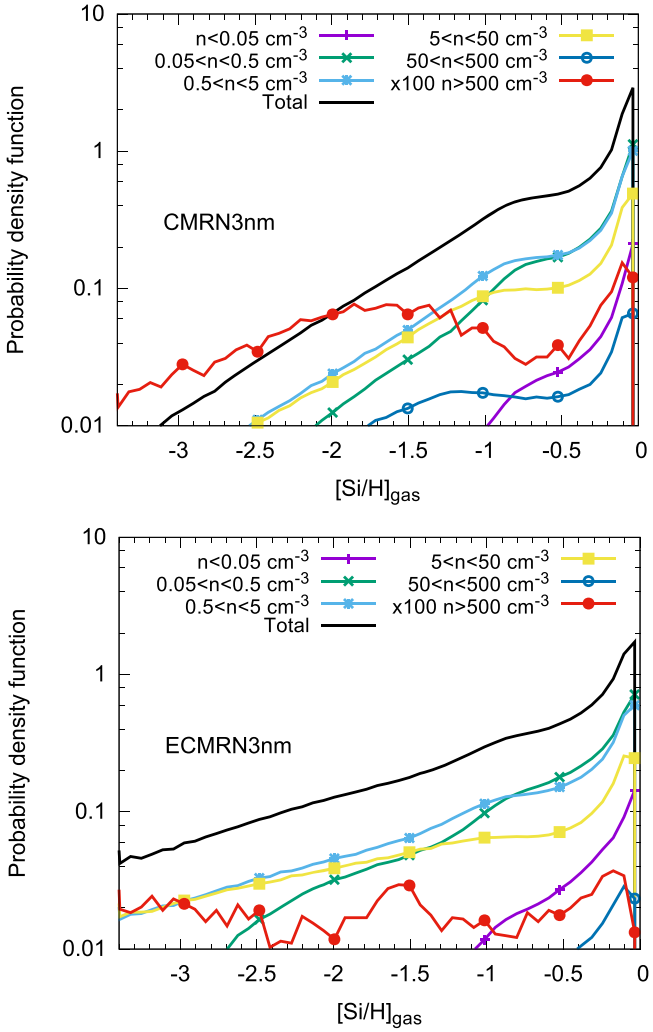

Figure 7. Probability density functions of the Si depletions per unit log depletion for the final simulation snapshot split into different gas density intervals spanning from 0.05 to 500 cm^{-3} (solid lines with various symbols, as indicated). The black line shows the PDF for all densities. All PDFs are normalized to the total gas mass in the considered volume. The top and bottom panels display models CMRN3nm and ECMRN3nm, respectively.

that become shallower in higher gas density bins as a consequence of the dust growth. The increase is commensurate with the observed depletion trends discussed in detail in Section 5.4.

The broadest depletion distribution derived for the densities $n > 500$ cm^{-3} reflects rich dynamic histories of particles at these densities. Particles with the highest depletions belong to clouds that were formed or evolved from the disruption of larger clouds. They have spent a longer time at larger densities. On the other hand, the low-density tail of the PDF corresponds to gas that has recently undergone compression from the diffuse gas so that the depletion values have not yet substantially increased. The highly asymmetric profiles of the PDFs shown in Figure 7 with a steady increase toward the less severe depletions are a direct consequence of the additional dust destruction in the diffuse phase. The mean depletions for these PDFs nevertheless provide the best match to the observed depletion values.

For the selected minimum grain size of 3 nm, the enhanced collision rates due to electrostatic focusing modestly affect the

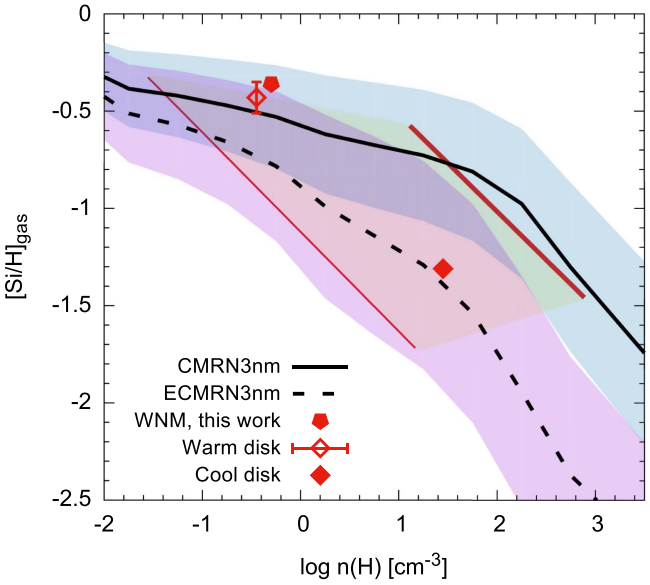

Figure 8. Relation between mean Si depletion and gas density derived using the final PDFs of gas-phase Si abundances for models CMRN3nm and ECMRN3nm (solid and dashed black lines, respectively). The shaded areas around the synthetic relations indicate the corresponding standard deviations. The pentagon symbol indicates a generalized depletion level at a location for a typical density of the WNM from observations. The thick red line shows the linear fit to the observed data given by Equation (20), and the thin red line shows the lower limit for this relation derived for the mean gas density on the line of sight given by Equation (19) (see explanation in Section 4). The yellow area shows the range of values between two relations. Typical values for the warm and cool galactic disk (open and solid diamond, respectively) derived by Savage & Sembach (1996a) are shown for comparison.

PDFs of Si depletion (Figure 7, bottom panel). This process is responsible for the shallower slopes of PDFs for the density range $0.05\,\mathrm{cm}^{-3} < n \leqslant 50\,\mathrm{cm}^{-3}$ owing to the enhanced growth under these conditions. The PDF for $n > 50\,\mathrm{cm}^{-3}$ looks lower for the ECMRN3nm model because a larger fraction of gas at these densities has Si depletion values below -3.5.

5.4. Si Depletion–Gas Density Relation

In order to compare our model predictions with the observed relation between Si depletion and gas density (Section 4), we compute the mean values and standard deviations of the interstellar Si depletion using the PDFs for the final simulation snapshot. For this analysis, the PDFs are computed in the same way as described in the previous section, but within much finer logarithmic gas density intervals. The resulting relations between the gas-phase Si abundance and gas density are shown in Figure 8 for reference models ECMRN3nm and CMRN3nm, in which a simple step function is adopted for the sticking coefficient ($\alpha = 1$ for $T_{\rm gas} < 300\,\mathrm{K}$ and $\alpha = 0$ for higher $T_{\rm gas}$).

Figure 8 also shows the relations between the mean $[\mathrm{Si_{gas}/H}]$ values and the gas density derived from observations. The relation based on the gas densities probed by C I fine-structure lines (Equation (19)) is limited to a narrow density range of 10–$10^3\,\mathrm{cm}^{-3}$. A generalized Si depletion level in the WNM inferred from observations provides a constraint for dust evolution models in the WNM density regime. Additionally, Figure 8 shows the relation derived for the mean gas density on the lines of sight given by Equation (19), which we consider as a lower limit to the observed relation.

A conspicuous feature of the synthetic mean $[\mathrm{Si_{gas}/H}]$–$n\,(\mathrm{H})$ relation for all models is the large standard deviation of about 0.5 dex at the lowest gas densities up to one dex at higher densities. These large variations predicted by the dust evolution models agree well with the dispersion in the real $[\mathrm{Si_{gas}/H}]$ values from observations (Figure 2). The dispersion arises from different dynamical histories of gas parcels with the same density that undergo various stages of the life cycle of GMCs. Gas that previously resided in GMCs on its way to the WNM has higher Si depletions, while matter from the WNM has lower element depletions because of the dust destruction process. This effect can also be seen in the widths of the PDFs calculated within the larger density bins discussed above.

Another characteristic feature of the synthetic mean $[\mathrm{Si_{gas}/H}]$–$n\,(\mathrm{H})$ relation is its different slopes at the low and high gas densities, seen as the double power law in Figure 8. The slope in the dense gas regime is steeper, and its value of 0.5 is in excellent agreement with the slope of the observed relation. This agreement provides the evidence of dust growth by accretion in the ISM. With enhanced collision rates due to ion–grain interactions (model ECMRN3nm), the accretion timescale is shorter, and the slope in the diffuse gas is therefore steeper compared to the CMRN3nm model.

A comparison of the slopes at low densities for models ECMRn3nm and CMRN3nm reveals that this slope also depends on the accretion timescale, although the growth is limited to temperatures below 300 K in these models. This is also supported by the fact that dust destruction in the diffuse phase does not depend on the local density in our model. The slope in the low-density regime is determined by the dust depletion at high densities, which is controlled by the growth timescale. An additional important factor controlling the distribution of dust abundances at low densities is the mass circulation between the GMCs and the diffuse medium. In this work, it is set by numerical simulations of GMC evolution and is the same in both dust models, so the differences in the slope at low densities between models CMRN3nm and EMRN3nm, as well as in other models discussed in the remainder of this paper, are the "memory" of dust growth by accretion at higher densities.

In the reference models described above, we include dust destruction in the diffuse ISM in addition to destruction by type II SNe in GMCs. We compare the synthetic relations between $[\mathrm{Si_{gas}/H}]$ and $n\,(\mathrm{H})$ obtained from the reference models with those from models MRN3nm and EMRN3nm in Figure 9. All parameters are the same with the exception of dust destruction, which in models MRN3nm and EMRN3nm occurs only through feedback from massive stars in GMCs. Models without additional destruction in the diffuse ISM overpredict Si depletion by 0.5 dex in the case without ion–grain interactions included and by 1 dex in the model EMRN3nm with enhanced collision rates due to ion–grain interactions.

The observed distribution of gas-phase element abundances thus implies that some fraction of stellar feedback energy is injected into the diffuse medium. SN energy input only in the dense phase results in too-low $[\mathrm{Si_{gas}/H}]$ values compared to the observations. The importance of stellar feedback energy injection in the diffuse ISM is also stressed in the work by Walch et al. (2015), who analyze how the location of SN explosions affects the structure of the ISM by means of high-resolution hydrodynamical simulations of the ISM.

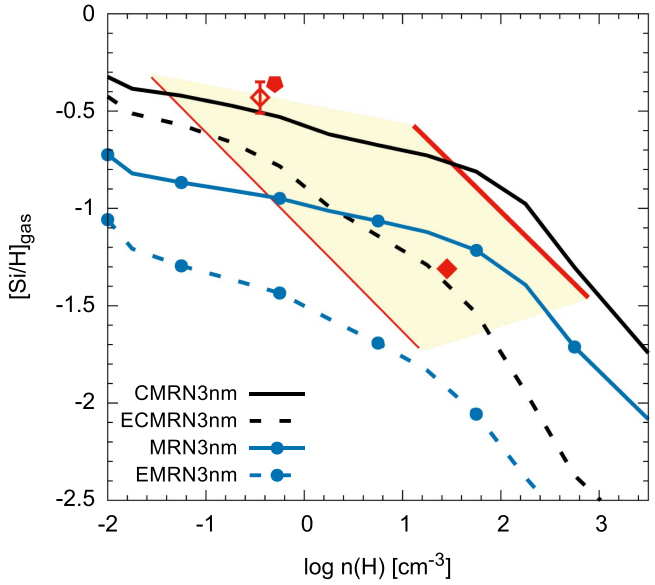

Figure 9. Same as in Figure 8 compared to the relations between mean Si depletion and gas density derived for models MRN3nm and EMRN3nm (blue solid and dashed lines with circles, respectively) without additional dust destruction in the diffuse ISM. To aid clarity, we do not show the standard deviations for the synthetic relations.

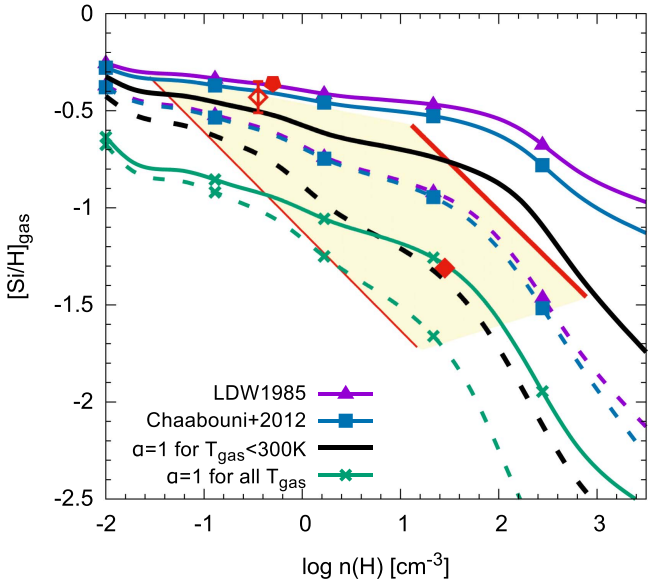

Figure 10. Relation between Si depletion and gas density derived using the PDFs of gas-phase Si abundances for the final snapshot in the simulations for different sticking coefficients: α from the work of Leitch-Devlin & Williams (1985) and Chaabouni et al. (2012) and $\alpha = 1$ (lines with triangles, squares, and crosses, respectively). The solid and dashed lines show models CMRN3nm and ECMRN3nm, respectively. The observational data are displayed in the same way as in Figure 8.

The present dust evolution model does not include dust and gas input from stars. Since the volume-filling factor of the diffuse medium is much larger than that of the molecular clouds, evolved stars inject matter mainly in the diffuse phase. For the stardust evolution model of Zhukovska et al. (2008), the dust input rate from stars is significantly lower than the rate of dust mass growth in the ISM (see Section 5.1), and $[Si_{gas}/H]$ in the stellar ejecta is higher than the observed value in the warm phase. Therefore, adding stellar dust sources self-consistently would result in slightly higher values of $[Si_{gas}/H]$ in the diffuse gas but would not change the slope of the $[Si_{gas}/H]$–n(H) relation.

In this work, we focus on the matter cycle at the solar galactocentric radius. Dobbs & Pringle (2013) demonstrate that the dominant mechanisms of disruption and formation of the GMCs are different in the outer and inner disk. Clouds in the inner disk are more likely to get destroyed by stellar feedback and shear, while large-scale gas dynamics is more important at the larger radii. The radial distribution of dust and, correspondingly, element depletions in the gas phase are affected by the changes in dynamical evolution of GMCs with distance from the Galactic center, in addition to the metallicity radial gradients. Our preliminary study indicates that shorter lifetimes of the clouds in the outer disk result in lower element depletions. We investigate how the radial variations in the dynamical evolution of clouds impact the dust abundances and the $[Si_{gas}/H]$–n(H) relation in a forthcoming paper.

5.5. Observational Constraints for the Sticking Coefficient

The sticking coefficient affects the final distribution of the interstellar depletions by limiting the densities of the ISM at which dust mass can grow by accretion of gas-phase species. In order to analyze how the modeled depletions depend on the choice of the sticking coefficient, we perform the simulations for models with the same parameters as ECMRN3nm and CMRN3nm but assuming different α as discussed in Section 3.3.2. The resulting relations for the mean depletion as a function of gas density are shown in Figure 10.

The reference model includes the dust growth only for $T_{gas} < 300$ K with the maximum value of $\alpha = 1$. If the temperature restriction is lifted, the theoretical $[Si_{gas}/H] - \log n$(H) relation shifts by -0.3 at low densities and by -0.8 at high densities. To balance dust growth at high temperatures and to lower depletions in the diffuse ISM in models MRN3nm and EMRN3nm to the observed level would require an unreasonably short timescale τ_{dest}^{diff} of destruction in the diffuse medium in Equation (16). We therefore conclude that the assumption of the maximum coefficient for all temperatures, commonly used in recent hydrodynamical simulations with dust (e.g., Bekki 2015a, 2015b; McKinnon et al. 2016), tends to overestimate the dust production rates in hydrodynamic numerical simulations of galactic evolution.

The sticking coefficients derived by Chaabouni et al. (2012) and by Leitch-Devlin & Williams (1985) have different dependences on the gas temperature. The latter has a maximum at about 200 K, while the former peaks at $T_{gas} \sim 10$ K. The fact that both prescriptions result in similar $[Si_{gas}/H] - \log n$(H) relations reveals that the mean depletions are not very sensitive to the choice of α, as long as it decreases with gas temperature. CMRN3nm models with α from Chaabouni et al. (2012) and Leitch-Devlin & Williams (1985) yield too-high $[Si_{gas}/H]$ values and a shallower slope than the values from the observational data. The calculations for the EMRN3nm models provide a better fit to the observations than that for the CMRN3nm model.

5.6. Dependence on the Grain Size Distribution

In the previous sections we discussed various results of dust modeling for a fixed grain size distribution. The size distribution for silicate grains, in particular its lower limit, is

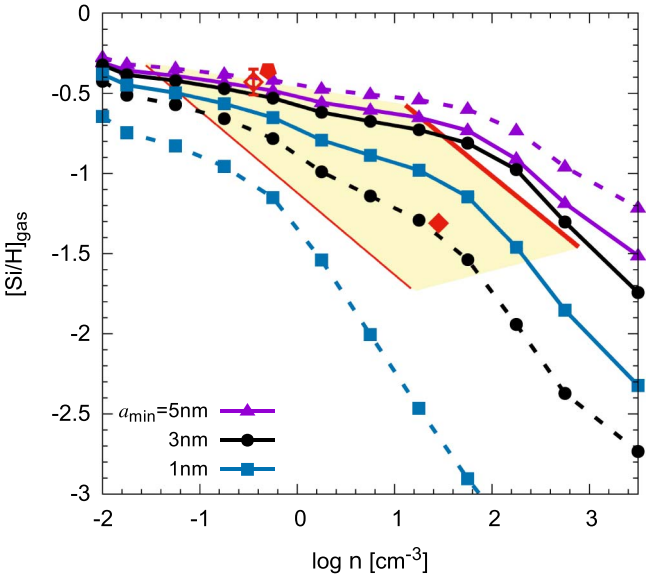

Figure 11. Relation between Si depletion and gas density derived from the final distribution of Si gas-phase abundances in the simulations for minimum grain size $a_{\rm min} = 1$, 3, and 5 nm (lines with squares, circles, and triangles, respectively) for the CMRN and ECMRN models (solid and dashed lines, respectively). The observed relation is shown in the same way as in Figure 8.

a highly uncertain parameter and varies among different models. It is determined by fitting the observed spectral energy distribution of interstellar dust in the diffuse medium (Zubko et al. 2004; Siebenmorgen et al. 2014). The grain size distribution enters the rate of the dust growth in the ISM via Equations (5)–(9). Variations in the grain sizes affect the final element depletions through the change in the total surface area and through enhanced collision rates with smaller grains (Weingartner & Draine 1999).

In the following, we inspect how the variations in the lower limit of the grain size distribution affects the relation between the average Si depletion and gas density predicted by our models. We use the same value $a_{\rm max} = 0.5$ μm for the upper limit for the grain sizes, as it has little effect on the total surface area. All other parameters are taken to be the same as for the reference model. The results for models CMRN and ECMRN with $a_{\rm min} = 1$, 3, and 5 nm for the final simulation snapshot are shown in Figure 11.

The synthetic average $[{\rm Si_{gas}/H}]$ versus $\log n({\rm H})$ relations show the double power-law behavior noted above for the reference models. With the decrease of the minimum grain size, the total surface area of grains increases and the accretion in the ISM occurs faster, resulting in steeper slopes of the relation and a transition to the efficient growth phase at lower densities. This effect is additionally enhanced by the presence of negatively charged small grains if the collision rates of grains with ions are included (see Figure 1 in Weingartner & Draine 1999). The differences in Si depletion values between the ECMRN and CMRN models may reach 1 dex at high densities for $a_{\rm min} = 1$ nm and $a_{\rm min} = 3$ nm (Figure 11). The ratio of the gas densities at which the transition to effective growth takes place roughly corresponds to the ratio of the growth timescales that for the models shown in Figure 11 is determined by the average grain radius $\langle a \rangle_3$ (Table 2).

Recently, Ferrara et al. (2016) suggested that the Coulomb repulsion between charged grains and ions prevents the growth by accretion in the diffuse ISM at galaxies at high redshifts. In such galaxies, the intensity of the interstellar UV radiation field and grain charges are significantly larger than in the present Milky Way. We do not find that the Coulomb barrier blocks the dust growth in the local Galaxy. In contrast, growth by accretion in the CNM occurs even for the assumption of the "classical" cutoff of the MRN size distribution $a_{\rm min} = 5$ nm, since only silicate grains larger than 20 nm are positively charged (Weingartner & Draine 1999). In this case, however, repulsion between ions and positively charged grains results in a somewhat longer accretion timescale and shallower slopes of the depletion–gas density relation than in model CMRN5nm. The mean $[{\rm Si_{gas}/H}]$ values in the dense gas for models CMRN5nm and ECMRN5nm are higher than the observational data (Figure 11); we therefore favor the models with $a_{\rm min} = 3$ nm.

We conclude that silicate grains with sizes that are smaller than the cutoff of the MRN size distribution of $a_{\rm min} = 5$ nm are necessary to reproduce the observed slope of the $[{\rm Si_{gas}/H}]-\log n({\rm H})$ relation in our model. Underlying this result is the assumption that some chemical selection process prevents sticking of Si on very small carbonaceous grains, such as desorption upon photoexcitation by UV irradiation (Tielens 1998; Draine 2009).

We do not take into account that the grain size distribution evolves in dense cores of molecular clouds owing to a coagulation process. Hirashita (2012) showed that because element depletion by accretion occurs at lower gas densities than grain coagulation, the reduction of total grain surface area by coagulation only slightly affects the dust mass growth in the ISM. Indeed, we find that efficient dust growth occurs already in the CNM and consumes almost all gas-phase Si at much higher densities than the coagulation regime ($\gtrsim 10^4$ cm^{-3}).

6. CONCLUSIONS

We develop a 3D model for interstellar dust evolution as traced by Si abundance based on numerical hydrodynamical simulations of GMCs in a Milky Way–like galaxy. This work focuses on the model predictions in a ring centered on the solar galactocentric radius so that they can be tested against the gas-phase Si abundances measured along numerous sight lines and probing various interstellar conditions in the local Milky Way. Combining the depletion data with measurements of the local gas density from fine-structure lines of neutral carbon, we derive a relation between the average Si abundance in the gas $[{\rm Si_{gas}/H}]$ and the local gas density $n({\rm H})$ that we use as a critical constraint for the models.

We demonstrate that the present rate of dust re-formation in the ISM of 0.1 $M_\odot$ Gyr^{-1} pc^{-2} in the solar neighborhood is substantially larger than the dust injection rate by stars (0.003 $M_\odot$ Gyr^{-1} pc^{-2}). Most dust growth occurs in the density range 5 cm^{-3} $< n \leqslant$ 50 cm^{-3}, accounting for one-half of the total growth rate. We find that the dust mass growth takes place in the CNM for all considered values of the minimum grain size $a_{\rm min}$ from 1 to 5 nm, despite the Coulomb repulsion between positively charged impinging ions and large, positively charged grains. Because of the presence of negatively charged small grains, the accretion timescale for $a_{\rm min} \lesssim 3$ nm is shorter when accounting for Coulomb interactions.

The model includes the destruction of grains by energetic feedback from SNe that occur mostly in the GMCs in the hydrodynamical simulations used for the dust modeling. This destruction process has a relatively long timescale of 1 Gyr,

resulting in overpredicted dust abundances in the WNM compared to observations. The latter constraint can only be reproduced with the implementation of an additional destruction process in the diffuse ISM representing noncorrelated SNe from runaway massive stars and SNe Ia. We derive an average lifetime of silicate grains against destruction of 350 Myr for our best-fit model. Our findings reinforce the assumption that the destruction of grains by single SNe exploding in the diffuse ISM is a dominant pathway of dust destruction.

We calculate the probability density distributions of the $[Si_{gas}/H]$ and their corresponding mean values and standard deviations for different gas densities. The resulting relation between the average $[Si_{gas}/H]$ and the gas density derived for the dust distribution at the end of the simulations is used to constrain the dust growth model by comparison with the observed relation. We find that the assumption of a constant sticking coefficient adopted in recent hydrodynamics models with dust significantly overestimates the dust growth rates. The observed $[Si_{gas}/H]-\log n(H)$ relation requires a sticking coefficient that decreases with temperature. A simple assumption that the growth is limited to the CNM and clouds with $T < 300$ K provides a slightly better fit in the CNM density range than the provisional models with temperature-dependent sticking coefficients from Chaabouni et al. (2012) and Leitch-Devlin & Williams (1985). Including the enhanced collision rates of cations with grains in the CNM and adopting the lower limit for the grain size of $\lesssim$3 nm in the dust growth model are crucial to reproducing the observed slope of the $[Si_{gas}/H]-\log n(H)$ relation.

The dust evolution model proposed in this work does not require the presence of a population of very small silicate grains like the one known to exist for carbonaceous grains (Draine & Anderson 1985; Draine & Li 2001). Including the 1 nm grains in the model leads to overly high Si depletions in the entire simulation volume. If such a population exists, then an additional mechanism, other than sputtering in SN shocks, has to be included in the model to remove accreted Si from the grain surfaces and provide the observed levels of Si depletion in the ISM.

S.Z. acknowledges support by the Forschungsgemeinschaft through SPP 1573: "Physics of the Interstellar Medium." We are grateful to Nikolai Voshchinnikov and Simon Glover for reading the manuscript. We thank the referee for useful comments that helped to improve the manuscript. We gratefully acknowledge the Max Planck Computing and Data Facility for providing their user support and computing time on the Odin and Hydra clusters. C.D. acknowledges support by the European Research Council under the European Community's Seventh Framework Programme (FP7/2011-2016 grant agreement No. 280104, LOCALSTAR). R.S.K. thanks for support from the DFG via 1573: "Physics of the Interstellar Medium" and via SFB 881: "The Milky Way System" (subprojects B1, B2, and B8), and from the European Research Council via the ERC Advanced Grant STARLIGHT (project number 339177). The findings reported in Section 4 of this paper arose from conclusions supported by *HST* archival program No. 09534 and 10279, which were provided by NASA through grants from the Space Telescope Science Institute (STScI), which is operated by the Association of Universities for Research in Astronomy, Incorporated, under NASA contract NAS5-26555.

REFERENCES

Asano, R. S., Takeuchi, T. T., Hirashita, H., & Inoue, A. K. 2013a, EP&S, 65, 213
Asano, R. S., Takeuchi, T. T., Hirashita, H., & Nozawa, T. 2013b, MNRAS, 432, 637
Bate, M. R., Bonnell, I. A., & Price, N. M. 1995, MNRAS, 277, 362
Bekki, K. 2013, MNRAS, 436, 2254
Bekki, K. 2015a, ApJ, 799, 166
Bekki, K. 2015b, MNRAS, 449, 1625
Benz, W., Cameron, A. G. W., Press, W. H., & Bowers, R. L. 1990, ApJ, 348, 647
Binney, J., & Tremaine, S. 1987, The Galactic dynamics (Princeton, NJ: Princeton Univ. Press)
Bocchio, M., Jones, A. P., & Slavin, J. D. 2014, A&A, 570, A32
Calura, F., Pipino, A., & Matteucci, F. 2008, A&A, 479, 669
Calzetti, D. 2013, in Secular Evolution of Galaxies, ed. J. Falcón-Barroso & J. H. Knapen (Cambridge: Cambridge University Press), 419
Chaabouni, H., Bergeron, H., Baouche, S., et al. 2012, A&A, 538, A128
Christensen, C., Quinn, T., Governato, F., et al. 2012, MNRAS, 425, 3058
Cox, D. P., & Gomez, G. C. 2002, ApJS, 142, 261
Dartois, E., Mu Oz. Caro, G. M., Deboffle, D., & D'hendecourt, L. 2004, A&A, 423, L33
de Bennassuti, M., Schneider, R., Valiante, R., & Salvadori, S. 2014, MNRAS, 445, 3039
D'Hendecourt, L. B., Allamandola, L. J., & Greenberg, J. M. 1985, A&A, 152, 130
Dobbs, C. L. 2008, MNRAS, 391, 844
Dobbs, C. L., Burkert, A., & Pringle, J. E. 2011, MNRAS, 417, 1318
Dobbs, C. L., & Pringle, J. E. 2013, MNRAS, 432, 653
Dorschner, J., & Henning, T. 1995, A&ARv, 6, 271
Draine, B. T. 1990, in ASP Conf. Ser. 12, The Evolution of the Interstelllar Medium, ed. L. Blitz (San Francisco, CA: ASP), 193
Draine, B. T. 2009, in ASP Conf. Ser. 414, Cosmic Dust—Near And Far, ed. T. Henning, E. Grün, & J. Steinacker (San Francisco, CA: ASP), 453
Draine, B. T., & Anderson, N. 1985, ApJ, 292, 494
Draine, B. T., & Li, A. 2001, ApJ, 551, 807
Draine, B. T., & Salpeter, E. E. 1979, ApJ, 231, 438
Dwek, E. 1998, ApJ, 501, 643
Dwek, E. 2005, in AIP Conf. Proc. 761, The Spectral Energy Distributions of Gas-Rich Galaxies: Confronting Models with Data, ed. C. Popescu & R. Tuffs (Melville, NY: AIP), 103
Dwek, E., Galliano, F., & Jones, A. P. 2007, ApJ, 662, 927
Dwek, E., & Scalo, J. M. 1980, ApJ, 239, 193
Ferrara, A., Viti, S., & Ceccarelli, C. 2016, MNRAS, 463, 112
Ferrarotti, A. S., & Gail, H.-P. 2006, A&A, 447, 553
Fitzpatrick, E. L., & Massa, D. 2007, ApJ, 663, 320
Forbes, J. C., Krumholz, M. R., Goldbaum, N. J., & Dekel, A. 2016, Natur, 535, 523
Glover, S. C. O., & Mac Low, M.-M. 2007, ApJS , 169, 239
Grassi, T., Krstic, P., Merlin, E., et al. 2011, A&A, 533, 123
Haris, U., Parvathi, V. S., Gudennavar, S. B., et al. 2016, AJ, 151, 143
Hirashita, H. 1999, ApJ, 522, 220
Hirashita, H. 2012, MNRAS, 422, 1263
Hirashita, H., & Kuo, T.-M. 2011, MNRAS, 416, 1340
Hirashita, H., Nozawa, T., Villaume, A., & Srinivasan, S. 2015, MNRAS, 454, 1620
Hollenbach, D., & Salpeter, E. E. 1971, ApJ, 163, 155
Hu, C.-Y., Naab, T., Walch, S., Glover, S. C. O., & Clark, P. C. 2016, MNRAS, 458, 3528
Jenkins, E. B. 1987, in Proc. Interstellar Processes Symp. 134, ed. D.-J. Hollenbach & H.-A. Thronson, Jr. (Dordrecht: Reidel), 533
Jenkins, E. B. 2009, ApJ, 700, 1299
Jenkins, E. B. 2013, ApJ, 764, 25
Jenkins, E. B., Savage, B. D., & Spitzer, L. J. 1986, ApJ, 301, 355
Jenkins, E. B., & Tripp, T. M. 2011, ApJ, 734, 65
Jones, A., Tielens, A., & Hollenbach, D. 1996, ApJ, 469, 740
Jones, A. P., Tielens, A. G. G. M., Hollenbach, D. J., & McKee, C. F. 1994, ApJ, 433, 797
Joseph, C. 1988, ApJ, 335, 157
Joseph, C. L., Snow, T. P., Seab, C. G., & Crutcher, R. M. 1986, ApJ, 309, 771
Klessen, R. S., & Glover, S. C. O. 2016, Star Formation in Galaxy Evolution: Connecting Numerical Models to Reality, Saas-Fee Advanced Course, Vol. 43 (Berlin: Springer)
Krasnokutski, S. A., Rouillé, G., Jäger, C., et al. 2014, ApJ, 782, 15
Leitch-Devlin, M. A., & Williams, D. A. 1985, MNRAS, 213, 295

Lodders, K. 2003, ApJ, 591, 1220
Lodders, K., Palme, H., & Gail, H.-P. 2009, in Solar System, ed. J. E. Trümper (Berlin: Springer)
Mathis, J. S., Rumpl, W., & Nordsieck, K. H. 1977, ApJ, 217, 425
Mattsson, L., & Andersen, A. C. 2012, MNRAS, 423, 38
McKee, C. 1989, in IAU Symp. 135, Interstellar Dust, ed. L. J. Allamandola & A. G. G. M. Tielens (Dordrecht: Kluwer), 431
McKinnon, R., Torrey, P., & Vogelsberger, M. 2016, MNRAS, 457, 3775
Mihalas, D., & Binney, J. 1981, Galactic Astronomy: Structure and Kinematics (2nd ed.; San Francisco, CA: Freeman)
O'Donnell, J. E., & Mathis, J. S. 1997, ApJ, 479, 806
Oey, M. S., & Lamb, J. B. 2012, in ASP Conf. Ser. 465, Four Decades of Research on Massive Stars, ed. L. Drissen et al. (San Francisco, CA: ASP), 431
Press, W. H., Teukolsky, S. A., Vetterling, W. T., & Flannery, B. P. 2007, Numerical Recipes: The Art of Scientific Computing (3rd ed.; Cambridge: Cambridge Univ. Press)
Price, D. J., & Monaghan, J. J. 2007, MNRAS, 374, 1347
Reach, W. T., Heiles, C., & Bernard, J.-P. 2015, ApJ, 811, 118
Rémy-Ruyer, A., Madden, S. C., Galliano, F., et al. 2014, A&A, 563, A31
Roman-Duval, J., Gordon, K. D., Meixner, M., et al. 2014, ApJ, 797, 86
Rouillé, G., Jäger, C., Krasnokutski, S. A., Krebsz, M., & Henning, T. 2014, FaDi, 168, 449
Roy, A., Martin, P. G., Polychroni, D., et al. 2013, ApJ, 763, 55
Santini, P., Maiolino, R., Magnelli, B., et al. 2014, A&A, 562, A30
Savage, B. D., & Sembach, K. R. 1996a, ARA&A, 34, 279
Savage, B. D., & Sembach, K. R. 1996b, ApJ, 470, 893
Seab, C. G., & Shull, J. M. 1983, ApJ, 275, 652
Serra Díaz-Cano, L., & Jones, A. P. 2008, A&A, 492, 127
Siebenmorgen, R., Voshchinnikov, N. V., & Bagnulo, S. 2014, A&A, 561, A82
Slavin, J. D., Dwek, E., & Jones, A. P. 2015, ApJ, 803, 7
Spitzer, L. J. 1985, ApJL, 290, L21
Spitzer, L. J., & Jenkins, E. B. 1975, ARA&A, 13, 133
Tielens, A. G. G. M. 1998, ApJ, 499, 267
Voshchinnikov, N. V., & Henning, T. 2010, A&A, 517, A45
Walch, S., Girichidis, P., Naab, T., et al. 2015, MNRAS, 454, 238
Watson, W. D., & Salpeter, E. E. 1972, ApJ, 174, 321
Weingartner, J., & Draine, B. 1999, ApJ, 517, 292
Weingartner, J. C., & Draine, B. T. 2001, ApJS, 134, 263
Yozin, C., & Bekki, K. 2014, MNRAS, 439, 1948
Zhukovska, S. 2008, PhD thesis, Ruperto-Carola University
Zhukovska, S. 2014, A&A, 562, A76
Zhukovska, S., & Gail, H.-P. 2009, in ASP Conf. Ser. 414, Cosmic Dust Near and Far, ed. Th. Henning, E. Grün, & J. Steinacker (San Francisco, CA: ASP), 199
Zhukovska, S., Gail, H.-P., & Trieloff, M. 2008, A&A, 479, 453
Zhukovska, S., & Henning, T. 2013, A&A, 555, A99
Zubko, V., Dwek, E., & Arendt, R. G. 2004, ApJS, 152, 211